

# Equally sloped tomography with oversampling reconstruction

Jianwei Miao,<sup>1</sup> Friedrich Förster,<sup>2</sup> and Ofer Levi<sup>3</sup>

<sup>1</sup>*Department of Physics and Astronomy and California Nanosystems Institute, University of California, Los Angeles, California 90095-1547, USA*

<sup>2</sup>*Max-Planck-Institut fuer Biochemie, Abteilung Molekulare Strukturbiologie, Am Klopferspitz 18a, D-82152 Martinsried, Germany*

<sup>3</sup>*Department of Statistics, Stanford University, Stanford, California 94305-4065, USA*

(Received 4 May 2005; published 4 August 2005)

We report the development of equally sloped tomography for the reconstruction of a 3D object from a number of 2D projections. In a combination of pseudopolar fast Fourier transform and the oversampling method with an iterative algorithm, equally sloped tomography makes superior 3D reconstruction to conventional tomography that has an intrinsic drawback due to the use of equally angled 2D projections. We believe this general approach will find applications in x-ray imaging, electron microscopy, coherent diffraction microscopy, and other tomographic imaging fields.

DOI: [10.1103/PhysRevB.72.052103](https://doi.org/10.1103/PhysRevB.72.052103)

PACS number(s): 68.37.Yz, 87.59.Fm, 87.64.Ee

Tomography has made revolutionary impacts in a number of fields ranging from x-ray imaging, magnetic resonance imaging to electron microscopy.<sup>1-3</sup> Conventional tomography reconstructs a 3D object from a set of equally angled 2D projections. Since the set of projections are in polar coordinates and the object in Cartesian coordinates, interpolation has to be used in the reconstruction process, which introduces artifacts in the reconstructed 3D object. In application to biology, there are two more difficulties: a limited number of projections due to radiation damage to biological specimens<sup>4</sup> and, for electron microscopy, the missing wedge problem<sup>3</sup> (i.e., specimens cannot be tilted beyond  $\pm 70^\circ$  and the data in the remaining  $\pm 20^\circ$  projections are missing). These difficulties currently limit 3D imaging of cellular and organelle structures to a resolution of 5–6 nm.<sup>5</sup> In this letter, we developed equally sloped tomography to alleviate these difficulties. Unlike conventional tomography, the new approach makes use of a set of equally sloped projections. In a combination of pseudopolar fast Fourier transform (PPFFT) and the oversampling method with an iterative algorithm, equally sloped tomography makes mathematically exact 3D reconstruction when there is a sufficiently large number of equally sloped 2D projections, and more precise reconstruction than conventional tomography when there is a limited number of projections. Furthermore, the approach can in principle be applied to coherent diffraction microscopy by converting each 2D oversampled diffraction pattern to a 2D image and reconstructing a 3D object from a set of 2D images.<sup>6,7</sup>

PPFFT and its inversion algorithms were developed to make a fast Fourier transform relation of an object in a Cartesian grid with its Fourier slices in a pseudopolar grid.<sup>8</sup> Figure 1 shows the geometric construction for 2D PPFFT and its inversion, whereas the Z-axis is related by fast Fourier transform and, for simplicity, was ignored here. The object is an  $N \times N$  pixel array in a Cartesian grid. Its pseudopolar Fourier transform represents a set of  $2N$  solid lines with each having  $2N$  grid points, whereas each line represents a Fourier slice. The grid points are on a total of  $N$  concentric squares (dashed lines in Fig. 1). As the lines are equally sloped instead of equally angled, it is called a pseudopolar

instead of a polar grid. Since there are  $N \times N$  points in object space and  $2N \times 2N$  grid points in Fourier space, the 2D PPFFT algorithms use oversampled and equally sloped Fourier slices to retrieve the object and are hence algebraically exact, geometrically faithful and invertible where the equally sloped slices are used to perform exact trigonometric interpolation along the rows and columns of the concentric square grid. While we briefly described 2D PPFFT algorithms here, an extension to three dimensions has also been developed.<sup>8</sup>

Inverse PPFFT algorithm can in principle precisely convert Fourier slices in a pseudopolar grid to an object in a Cartesian grid, but requires two stringent conditions. For an object with  $N \times N$  pixels, the range of the rotation angles has to be between  $+90^\circ$  and  $-90^\circ$ , and the number of projections needs to be exactly  $2N$ . Moreover, pseudopolar Fourier slices are on a series of concentric square grids. But the Fourier slices calculated from the “measured” 2D projections are within a resolution circle, a circle inside the outer-most square and tangent to all four sides, shown in Fig. 2. The grid points between the resolution circle and the outermost square are inaccessible from the “measured” 2D projections. These conditions make the direct application of PPFFT to tomographic reconstruction difficult. In a combination of PPFFT

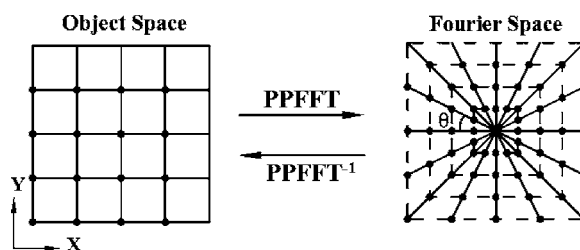


FIG. 1. Geometric construction for 2D PPFFT and its inversion. The object is in Cartesian coordinates with  $N \times N$  points where  $N = 4$  in this example. The grid points in Fourier space are on a set of concentric squares (i.e., dashed lines) with the number of squares equal to  $N$ . There are a total of  $2N$  solid lines with each having  $2N$  grid points, whereas each line represents a Fourier slice. The grid interval on each Fourier slice varies with  $\theta$  and is characterized by  $\alpha$  in Eq. (1).

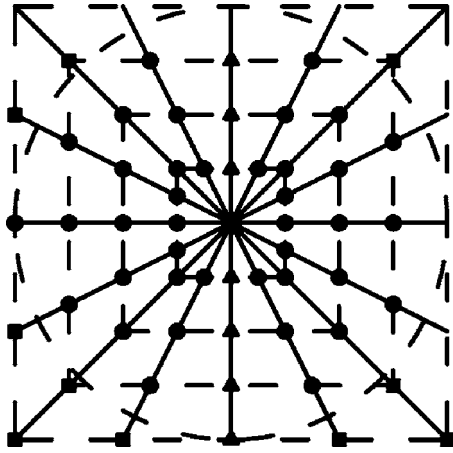


FIG. 2. Missing grid points due to a resolution circle. The grid points denoted by circles, which are within the resolution circle, represent the Fourier slices calculated from a limited number of “measured” projections. The grid points denoted by squares (outside the resolution circle) are inaccessible from the “measured” projections due to the resolution limitation. The grid points denoted by triangles represent a missing Fourier slice.

and the oversampling method with an iterative algorithm,<sup>9</sup> these difficulties can be overcome.

For a finite sized object, each Fourier slice is related to the object by the Fourier transform and the grid points on a Fourier slice are correlated to all the grid points on other Fourier slices. Here the concept of correlation can be understood that, if one grid point changes its value, the other points have to change accordingly and vice versa. When there are a limited number of slices and/or missing slices due to a missing wedge, some information about the object is permanently lost. However, if the correlated information can be extracted from the limited number of Fourier slices, the missing information of the object can be reduced to a minimum.

To extract the correlated information, we first obtained the oversampled Fourier slices in a pseudopolar grid from the limited number of “measured” projections by

$$F_{\theta}(u)|_{u \leq R} = \sum_{r=1}^L f_{\theta}(r) e^{-2\pi i r u / (2N\alpha)}$$

$$\alpha = \begin{cases} \sin(\theta) & \text{if } -45^{\circ} \leq \theta + 45^{\circ} \\ \cos(\theta) & \text{otherwise} \end{cases}, \quad (1)$$

where  $F_{\theta}(u)|_{u \leq R}$  represents the Fourier slices within the resolution circle,  $R$  is the radius of the circle,  $r$  and  $u$  are the radial coordinates in object and Fourier space,  $\theta$  is shown in Fig. 1,  $f_{\theta}(r)$  is the limited number of projections,  $\alpha$  is a parameter to characterize the grid interval on each Fourier slice, and  $L$  is an integer which is less than  $N$ . For simplicity the  $Z$ -axis is not shown here. Since oversampling the Fourier slices corresponds to surrounding the projections with mathematical zeros, we use the oversampling ratio ( $\sigma$ ), the total volume of the object and the region of zeros divided by the volume of the object, to characterize the oversampling degree.<sup>9</sup> The mathematical zeros do not provide extra information about the 3D object, but help to extract the correlated information among the 2D projections. While the requirement of  $\sigma \geq 2$  is crucial for phase retrieval of noncrystalline specimens,<sup>9</sup> our computer simulations have shown that it is not critical in tomographic reconstruction.

The limited number of Fourier slices were used to reconstruct the 3D object with an iterative algorithm, in which the  $j$ th iteration consists of the following steps: (i) A complete set of  $2N$  Fourier slices in a pseudopolar grid was obtained by updating  $G_{\theta}^{j-1}(u)$  with the limited number of “measured” Fourier slices [i.e.,  $F_{\theta}(u)|_{u \leq R}$ ], where  $G_{\theta}^{j-1}(u)$  represents a complete set of Fourier slices in the  $(j-1)$ th iteration. (ii) By using inverse PPFET, an object,  $g^j(x, y)$ , was computed. (iii) A new object was obtained by

$$\rho^j(x, y) = \begin{cases} g^j(x, y) & \text{if } (x, y) \in S \text{ and } g^j(x, y) \geq 0 \\ \rho^{j-1}(x, y) - \beta \times g^j(x, y) & \text{if } (x, y) \notin S \text{ or } g^j(x, y) < 0 \end{cases}, \quad (2)$$

where  $\beta$  is a constant between 0 and 1, and  $S$  represents a support separating the object from the region of zeros. The support is due to oversampling the Fourier slices. In this step, if a pixel is within the support and its value is non-negative, the pixel value remained unchanged. Otherwise, it was slowly pushed close to zero. (iv) By applying PPFET to  $\rho^j(x, y)$ , a new set of Fourier slices,  $G_{\theta}^j(u)$ , was obtained which would be used for the next iteration. (v) An error function was applied to monitor the reconstruction, which is the difference between the limited number of “measured” Fourier slices and the corresponding calculated ones in each iteration. For the first iteration,  $G_{\theta}^0(u)$  was obtained by mul-

tiplying a positive constant by a set of random phase angles. Our simulations have indicated that the algorithm is not sensitive to the initial condition.

We have carried out tomographic reconstruction of a simulated 3D biological vesicle of  $50 \times 26 \times 50$  voxels with internal structures. Figures 3(a)–3(c) show three central slices in the  $XY$ ,  $XZ$ , and  $ZY$  plane, respectively. A set of 27 projections were calculated from the 3D vesicle in which the rotation angles range from  $-70^{\circ}$  to  $+70^{\circ}$  and a missing wedge corresponds to  $\pm 20^{\circ}$ . The set of projections were converted to oversampled Fourier slices in a pseudopolar grid by using Eq. (1). A 3D object was reconstructed from the 27

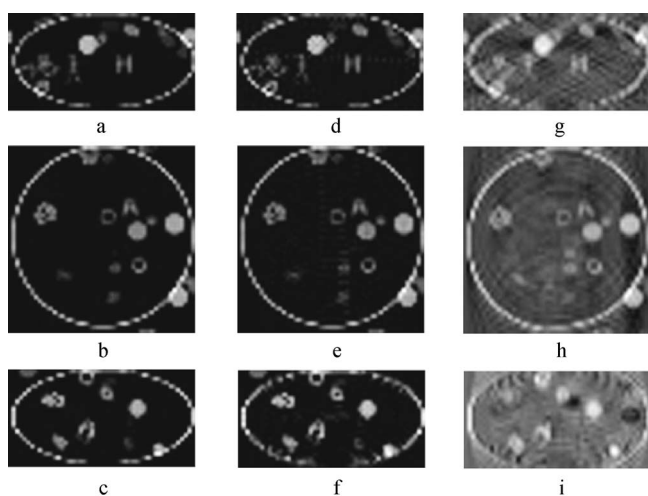


FIG. 3. Tomographic reconstruction of a simulated 3D biological vesicle. (a), (b), and (c) are the central slices in  $XY$ ,  $XZ$ , and  $YZ$  plane of the 3D vesicle. (d), (e), and (f) are the central slices of the vesicle reconstructed from 27 projections by using oversampling reconstruction. (g), (h), and (i) are the central slices reconstructed by using weighted backprojection of conventional tomography.

oversampled Fourier slices in which the overall array size in object space was  $64^3$  voxels, the support was a box with  $50 \times 26 \times 50$  voxels (i.e.,  $\sigma=4$ ), and the number of iterations and  $\beta$  were set to be 2000 and 0.9, respectively. Figures 3(d)–3(f) show the three central slices of the reconstructed 3D vesicle. For a comparison purpose, a 3D vesicle was reconstructed from the same 27 projections by using weighted back-projection shown in Figs. 3(g)–3(i), which is currently the most popular reconstruction algorithm for conventional tomography and was carried out by using the object diameter as a weighting parameter described elsewhere.<sup>10</sup> Figure 4 shows a quantitative comparison of the

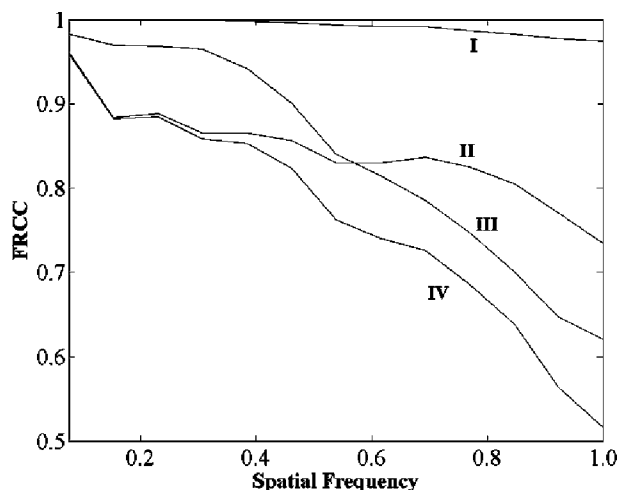


FIG. 4. A quantitative comparison of the reconstructions by using Fourier-ring correlation. Curves I and II correspond to the noise-free reconstructions by oversampling reconstruction and weighted back-projection. Curves III and IV correspond to the reconstructions with  $\text{SNR}=1$  by oversampling reconstruction and weighted back-projection.

two reconstructions by using Fourier-ring correlation,<sup>11</sup> which indicates that equally sloped tomography (curve I) performs far better than conventional tomography (curve II) in this case.

We carried out the study of noise on equally sloped tomography. In the simulations, we assumed that noise is uncorrelated to the signal in each projection and added Gaussian noise with a mean and a variance to each projection. We calculated the variance by dividing the variance of each projection by a signal-to-noise-ratio (SNR), and set the mean equal to 0. By using oversampling reconstruction, a 3D object was obtained from the 27 noisy projections with  $\text{SNR}=1$ . In the process,  $\beta$  and the number of iterations were set to be 0.0001 and 14, respectively as the error function did not improve after 14 iterations. A 3D object was also reconstructed from the same 27 noisy projections by using weighted backprojection. Figure 4 shows a Fourier-ring correlation comparison of the reconstructions by using oversampling reconstruction (curve III) and weighted backprojection (curve IV), which indicates that equally sloped tomography is superior to conventional tomography.

In some tomographic imaging applications, the 2D projections at different tilting angles image a slightly different part of a specimen shown in Fig. 5(a). The region of solid lines is imaged by all the projections, and the region of dotted lines by some of the projections, where  $Z$  is the rotation axis. To

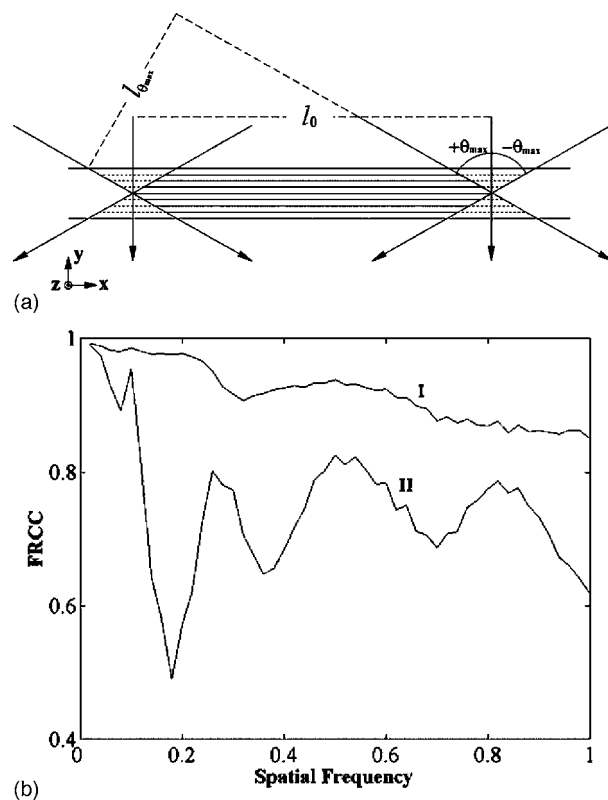


FIG. 5. (a) Geometric construction of specimen unboundedness where  $Z$  is the rotation axis. The region of solid lines is imaged by all the projections and the region of dotted lines by some of the projections. (b) A Fourier-ring correlation comparison of the reconstructions for an unbounded specimen by using oversampling reconstruction (curve I) and weighted back-projection (curve II).

simulate specimen unboundedness, we created a thin layer of vitreous ice with vesicles embedded inside. The size of the thin layer is  $256 \times 16 \times 100$  voxels. We calculated a set of 53 projections with each  $256 \times 100$  pixels, where the rotation angles range from  $-70^\circ$  to  $+70^\circ$  with a missing wedge corresponding to  $\pm 20^\circ$ . The set of projections were used to reconstruct the central part of the specimen ( $82 \times 16 \times 100$  voxels).

We developed an approximation method to deal with the specimen unboundedness problem. Since  $Z$  is the rotation axis, we can precisely determine the dimension of the object in both  $Y$  and  $Z$ -axis. The dimension in the  $X$ -axis was determined by

$$l_\theta = l_0 \times |\cos(\theta)|, \quad (3)$$

where  $l_0$ , shown in Fig. 5(a), is equal to 82 pixels in this case. Equation (3) is to reduce the effect of specimen unboundedness on the reconstruction. The new set of projections with size of  $l_\theta \times 100$  pixels was converted to oversampled Fourier slices with each  $128^2$  pixels in a pseudopolar grid. The iterative algorithm was used to reconstruct the central part of the specimen where the overall array size in object space is  $128^3$  voxels and the support is a box with  $128 \times 16 \times 100$  voxels. In the reconstruction, we enforced the constraint of zeros in both the  $Y$  and  $Z$ -axis, but not in the  $X$ -axis since the specimen was unbounded in that direction. The central part of the specimen was reconstructed after 300 iterations. For a comparison purpose, we used weighted backprojection to reconstruct the specimen from the 53 projections in which the dimension in the  $X$ -axis of each projection was not confined by Eq. (3). Figure 5(b) shows a quantitative comparison of the two reconstructions by using Fourier-ring correlation, which indicates that

equally sloped tomography performs far better than conventional tomography in this example.

Equally sloped tomography has been developed to reconstruct a 3D object from a set of equally sloped 2D projections. It is based upon the principle that all the Fourier slices are correlated and, by using PPFFT and the oversampling method with an iterative algorithm, the correlated information can be extracted to determine the 3D object. Our computer simulations have indicated that conventional tomography based upon equally angled projections has an intrinsic drawback that limits the quality of 3D reconstruction. By using equally sloped projections, the new approach can make superior 3D reconstruction to conventional tomography even with extremely high noise (i.e.,  $\text{SNR}=1$ ). Compared with other iterative algorithms,<sup>12–14</sup> equally sloped tomography is in principle more accurate due to the combination of PPFFT algorithms and oversampled Fourier slices with an iterative algorithm. The computing time for a  $64^3$  voxel array and one cycle of PPFFT and its inversion on a 1 GHz Pentium III laptop is about 19 s, which is not a limitation factor. We anticipate that equally sloped tomography will be applied to x-ray imaging,<sup>15–17</sup> electron microscopy,<sup>3,5</sup> coherent diffraction microscopy,<sup>6,7</sup> and other tomography fields.

We are grateful to K. O. Hodgson for his steady support to this research and D. Donoho for introducing the PPFFT algorithms to us. We thank D. Durkin for helping us carry out some computer simulations, and D. Donoho, R. Blankenbeler, M. Elad, Y. Nishino, A. Frangakis, and G. Jensen for many invaluable and stimulating discussions. This work was supported by the U.S. Department of Energy, Office of Basic Energy Sciences, and the Bundesministerium für Bildung und Forschung and the Stiftung Stipendien-Fonds der Chemischen Industrie (to F.F.).

<sup>1</sup>A. C. Kak and M. Slaney, *Principles of Computerized Tomographic Imaging* (SIAM, Philadelphia, 2001).

<sup>2</sup>F. Natterer and F. Wubbeling, *Mathematical Methods in Image Reconstruction* (SIAM, Philadelphia, 2001).

<sup>3</sup>J. Frank, *Electron Tomography* (Plenum, New York, 1992).

<sup>4</sup>R. Henderson, *Q. Rev. Biophys.* **28**, 171 (1995).

<sup>5</sup>O. Medalia, I. Weber, A. S. Frangakis, D. Nicastro, G. Gerisch, and W. Baumeister, *Science* **298**, 1209 (2002).

<sup>6</sup>J. Miao, T. Ishikawa, B. Johnson, E. H. Anderson, B. Lai, and K. O. Hodgson, *Phys. Rev. Lett.* **89**, 088303 (2002).

<sup>7</sup>I. K. Robinson and J. Miao, *MRS Bull.* **29**, 177 (2004).

<sup>8</sup>A. Averbuch, R. Coifman, D. Donoho, M. Israeli, and Y. Shkolnisky, *SIAM J. Sci. Comput. (USA)* (in press) (see preprint at <http://www.stat.stanford.edu/~donoho/Reports/2001/FastSlantStack.pdf>).

<sup>9</sup>J. Miao, H. N. Chapman, J. Kirz, D. Sayre, and K. O. Hodgson, *Annu. Rev. Biophys. Biomol. Struct.* **33**, 157 (2004).

<sup>10</sup>G. Harauz and M. van Heel, *Optik (Stuttgart)* **73**, 146 (1986).

<sup>11</sup>W. O. Saxton and W. Baumeister, *J. Microsc. (Paris)* **127**, 127 (1982).

<sup>12</sup>G. T. Herman and A. Kuba, *Proc. IEEE* **91**, 1612 (2003).

<sup>13</sup>J. Fernandez *et al.*, *J. Struct. Biol.* **138**, 6 (2002).

<sup>14</sup>P. A. Penczek, R. Renka, and H. Schomberg, *J. Opt. Soc. Am. A* **21**, 499 (2004).

<sup>15</sup>W. S. Haddad, I. McNulty, J. E. Trebes, E. H. Anderson, R. A. Levesque, and L. Yang, *Science* **266**, 1213 (1994).

<sup>16</sup>G. Schneider, E. Anderson, S. Vogt, C. Knochel, D. Weiss, M. LeGros, and C. Larabell, *Surf. Rev. Lett.* **9**, 177 (2002).

<sup>17</sup>K. A. Nugent, T. E. Gureyev, D. F. Cookson, D. Paganin, and Z. Barnea, *Phys. Rev. Lett.* **77**, 2961 (1996).